minerals

MDPI

Article

Multi-Proxy Study of a Holocene Soil Profile from Romania and Its Relevance for Speleothem Based Paleoenvironmental Reconstructions

Luchiana Faur [1,2], Virgil Drăguşin [1,3,*], Daniela Dimofte [2], Ferenc Lázár Forray [4], Maria Ilie [5,6], Constantin Marin [1], Cristian Mănăilescu [5], Ionuț Cornel Mirea [1], Cristian George Panaiotu [2], Barbara Soare [2], Alida Timar-Gabor [7] and Maria Laura Tîrlă [3,8]

1 Emil Racoviță Institute of Speleology, Frumoasă 31, 010986 Bucharest, Romania; luchiana.faur@iser.ro (L.F.); constmarin@gmail.com (C.M.); ionut.mirea@iser.ro (I.C.M.)
2 Faculty of Geology and Geophysics, University of Bucharest, N. Bălcescu 1, 010041 Bucharest, Romania; danidimofte@gmail.com (D.D.); cristian.panaiotu@gg.unibuc.ro (C.G.P.); barbara.soare@gg.unibuc.ro (B.S.)
3 Earth, Environmental and Life Sciences Division, Research Institute of the University of Bucharest, University of Bucharest, Panduri 90-92, 050663 Bucharest, Romania; tirla@geo.unibuc.ro
4 Department of Geology, Babes-Bolyai University, Kogălniceanu 1, 400084 Cluj-Napoca, Romania; ferenc.forray@ubbcluj.ro
5 Horia Hulubei National Institute for R&D in Physics and Nuclear Engineering, Reactorului 30, 077125 Măgurele, Romania; maria.ilie@nipne.ro (M.I.); cristian.manailescu@gmail.com (C.M.)
6 Doctoral School of Physics, Faculty of Physics, University of Bucharest, Atomistilor 405, 077125 Măgurele, Romania
7 Laboratory of Luminescence Dating and Dosimetry, Institute for Interdisciplinary Research in Bio-Nano-Sciences, Babeș-Bolyai University, 42 Treboniu Laurean, 400271 Cluj-Napoca, Romania; alida.timar@ubbcluj.ro
8 Faculty of Geography, University of Bucharest, N. Bălcescu 1, 010041 Bucharest, Romania
* Correspondence: virgil.dragusin@iser.ro

Citation: Faur, L.; Drăguşin, V.; Dimofte, D.; Forray, F.L.; Ilie, M.; Marin, C.; Mănăilescu, C.; Mirea, I.C.; Panaiotu, C.G.; Soare, B.; et al. Multi-Proxy Study of a Holocene Soil Profile from Romania and Its Relevance for Speleothem Based Paleoenvironmental Reconstructions. *Minerals* **2021**, *11*, 873. https://doi.org/10.3390/ min11080873

Academic Editor: Yuri Lopes Zinn

Received: 11 June 2021
Accepted: 9 August 2021
Published: 12 August 2021

Abstract: In this study, we describe a sedimentary deposit situated above Ascunsă Cave (SW Romania) that should be in depositional connection with coeval stalagmites from the cave. We excavated a 2.5 m deep soil profile and took contiguous bulk samples every 5 cm. Soil samples were analyzed for clay mineralogy, grain size, chemical composition, magnetic susceptibility, and stable carbon isotopes. Radiocarbon dating revealed that the soil is of Holocene age, and presents a depositional hiatus between 5.4 and 2.3 thousand years before the present. Due to the open system behavior of soils and mobility of organic matter, a few hundred years of uncertainty should be considered for the duration of this hiatus. The fine fraction is dominated by silt, while the clay mineralogical association is made of illite, chlorite, kaolinite, vermiculite, and illite–vermiculite and illite–chlorite mixed layered minerals. The sediment source of this soil is represented by a nearby mélange complex, as well as by an underlying terra rossa-type soil. As this latter type of soil is widespread in our study area, we performed luminescence dating on two samples from a representative location close to our site and it appears that this type of Mediterranean soil was formed during the Last Interglacial period. $\delta^{13}C$ variability in soil organic matter and a stalagmite from the cave are comparing well, and could help future studies identify modifications in isotopic fractionation processes within the cave.

Keywords: soil; clay minerals; Holocene; stable carbon isotopes; speleothems

1. Introduction

Holocene environmental changes in Central Eastern Europe were studied from a wide range of continental sedimentary archives such as peat accumulations and lake sediments [1–3], speleothems [4–6], cave ice accumulations [7,8] and guano deposits [9,10].

Speleothems are an important part of paleoenvironmental research and are intimately linked to the overlying soil cover. This relationship is based on organically derived CO_2 (from both root respiration and microbial decomposition of organic matter) and percolating water. Speleothems, which are chemical deposits formed from the precipitation of $CaCO_3$ from supersaturated percolating water, can be studied at very high resolution, annually or even seasonally [11,12]. Although soils are a highly heterogeneous deposit formed at the interface of the lithosphere, hydrosphere, atmosphere, and biosphere, they can archive a wealth of information regarding past environmental conditions [13]. Nevertheless, paleoenvironmental studies of speleothem–soil couples are not common.

Speleothem carbon isotopes are sourced from CO_2 resulting from root respiration and decomposition of organic matter on one hand, and from the carbonate host rock on the other hand. As the isotopic signature of the host rock is usually homogeneous, the variability of $\delta^{13}C$ in speleothems is given by plant and soil organic activity, being further influenced by isotopic fractionation within the karst system [14–16]. Thus, direct measurement of soil organic matter and speleothem $\delta^{13}C$ should allow for better constraining of isotopic fractionation processes inside the karst system.

Studies of stable isotope ratios from soil components, such as $\delta^{13}C$ of organic matter or $\delta^{2}H$ of hydrated minerals, have also been used to reconstruct temperature [17–19], precipitation [20,21], atmospheric pCO_2, or mean annual precipitations [22].

Other proxies such as clay mineralogy, chemical composition, magnetic susceptibility, or grain size can provide information about pedogenetic processes and local paleoenvironments [23–25]. The mineralogical composition of a soil is dependent on multiple factors such as parent material, vegetation cover, geomorphological features, the intensity of pedochemical weathering, and consequently the climate conditions [26].

This study proposes to investigate the soil above Ascunsă Cave (SW Romania) that should be in direct depositional connection with the POM 2 Holocene stalagmite [6] from the same cave. Knowing that stalagmite growth depends on soil organic activity as a source of CO_2, we intend to investigate if the environmental proxies in this soil are reworked, as compared to speleothems which usually behave as a closed system [14]. If soil proxies would be found to not have been reworked, then they can bring valuable complementary environmental information to accompany that from coeval speleothems. Here, we intend to offer a first assessment of the origin and characteristics of this soil, and to offer background information for several forthcoming studies, which will separately focus on organic compounds found in the POM 2 soil–stalagmite couple, metal concentrations in the soil–stalagmite couple, as well as carbon stable isotope fractionation within Ascunsă cave.

2. Study Site

The investigated sequence is located in the SW South Carpathians, on the eastern slope of Mehedinți Mountains above Ascunsă Cave, at ~1070 m altitude (Figure 1).

The lithology comprises a Neo-Proterozoic metamorphic basement with peridotites and amphibolites intruded by granitic bodies (Figure 2).

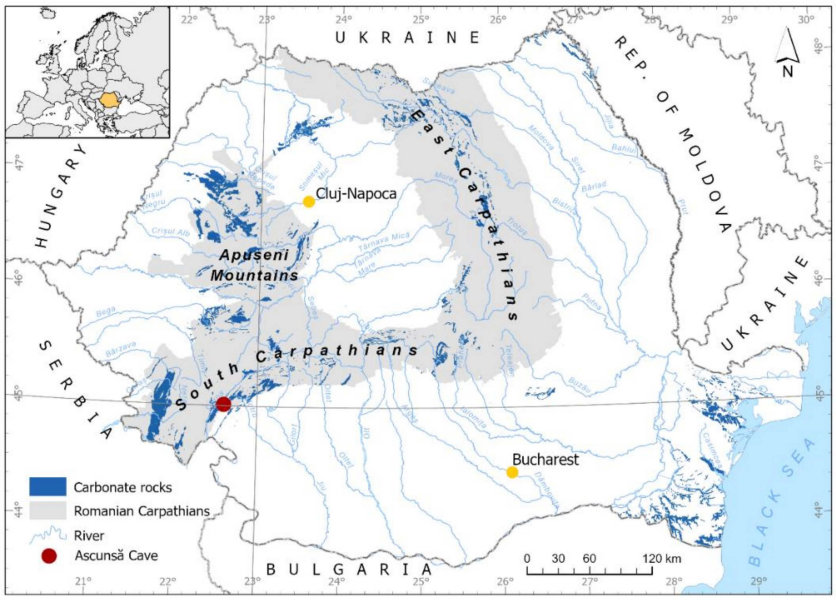

Figure 1. Location of study area modified from Bădescu & Tîrlă [27].

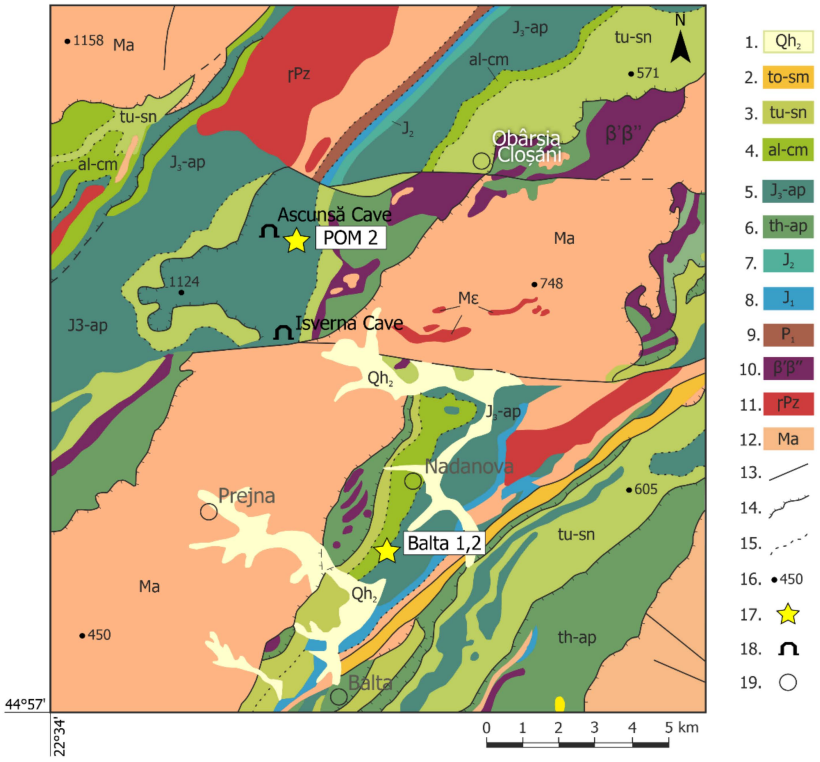

Figure 2. Geological map of the region (modified after Codarcea et al. [28]): 1. Quaternary: gravel and sand; 2. Tortonian–Sarmatian; 3. Turonian–Senonian mélange unit; 4. Albian–Cenomanian: marly limestones, sandstones and clays (Nadanova formation); 5. Upper Jurassic–Aptian: limestones, marly limestones (Sinaia beds); 6. Tithonian–Aptian: marly limestones, sandstones, conglomerates, dolerites; 7. Middle Jurassic: limestones, marly limestones, arkosic sandstones; 8. Lower Jurassic: conglomerates, sandstones, shales, coals; 9. Permian: conglomerates, sandstones, red shales; 10. Mesozoic and Permian migmatites: β'dolerite, β"-spilites; 11. Paleozoic magmatites and Precambrian granites; 12. Neoproterozoic: micaschists and gneisses; 13. Fault; 14. Thrust fault; 15. Lithologic limit; 16. Altimetry; 17. Soil profile; 18. Cave entrance; 19. Village.

The sedimentary cover in the region is made of conglomerates, sandstones and siltites of Lower Jurassic age (Hettangian–Aalenian), overlain by carbonate–siliciclastic rocks of Middle Jurassic age (Bajocian–Callovian) [29].

The Upper Jurassic–Lower Cretaceous interval is characterized by the development of a carbonate complex comprising micritic limestones and dolomites of Neocomian age that underlie Urgonian-type reef limestones of Barremian–Aptian age [30]. The sedimentary cover ends with a limestone/marl sequence of Cenomanian–Middle Turonian age, followed by the mélange complex made of terrigenous and volcanoclastic turbidites of Upper Turonian–Maastrichtian age [31].

Ascunsă cave was formed by an underground river that incised through erosion in the Turonian–Senonian mélange (wildflysch) unit, at the contact with the overlaying Barremian–Aptian limestones. The former outcrops on the walls for most of the length of the cave, while the latter forms the cave ceiling [6]. At the surface, the same mélange unit outcrops at a short distance uphill from the cave.

The climate of the area is humid continental (Dfb type in the Köppen–Geiger classification), the mean annual temperature at the site being close to 7 °C, while precipitation surpasses 700 mm/year. The soil cover is generally sparse, with frequent outcrops of limestone, and most of the soil being found within limestone fractures. The vegetation is represented by beech forests.

The sedimentary deposit studied here is hosted within a 2.5 m deep depression of unknown origin that might have resulted after the ceiling collapse of a cave passage. There is no apparent fluvial valley leading to or from this depression and it does not have the characteristics of a dissolution doline.

3. Materials and Methods

3.1. Mineralogical Analysis

The soil profile was sampled contiguously at a resolution of 5 cm, resulting in 50 samples (labeled POM 2-1 to POM 2-50, from top to bottom). For clay minerals analysis, samples were subject to separating treatments following the methods described in Kunze and Dixon [32] and Rabenhorst and Wilding [33].

In order to remove the organic matter, we treated samples with hydrogen peroxide and for carbonate removal with 4.5 pH buffer solution of acetic acid. Further, the remaining fine fraction has undergone saturation in Mg^{2+} and K^{+}, and ethylene-glycol solvation (EG). Measurements were made using a Malvern PanAlytical X'Pert Powder (Malvern, United Kingdom) conventional Bragg–Brentano vertical diffractometer with CuKα radiation, λ = 1.54 Å, 40 kV, 40 mA and a graphite monochromator. Data were recorded at a 0.01 °2θ step scanning, step time 10 s/step in the range 3 ÷ 33 °2θ.

HighScore© (2007) software version 2.2.3. was used for X-ray data analysis and PyXRD (v. 0.6.7.) [34] for clay modeling association. XRD identification of clay species was based on the indications of Biscaye [35], Brindley and Brown [36], and Moore and Reynolds [37].

Semi-quantitative mineral determination of clay minerals was based on the procedure described by Gjems [38] and updated by Soare [39]. We used the peak area provided by the High Score software and the correction factors (coefficient of proportionality, "C") of diagnostic peaks for each clay mineral as follows: illite ~ 10 Å peak area; C = 1. smectite ~16.5 Å peak area; C = 0.22. vermiculite ~ 14 Å peak area; C = 0.34. chlorite ~ 14 Å peak area; C = 0.34. kaolinite ~ 7 Å peak area; C = 0.24. interstratified—mica-illite/vermiculite (I/V) 12 Å peak area, C = 0.40; interstratified illite–chlorite (I/Chl) ~ 12 Å peak area; C = 0.40. Area reports were corrected using empirical crystallinity indices for each clay phase.

Furthermore, we analyzed six rock samples from the mélange formation which outcrops inside Ascunsă Cave. Samples were ground and measured using the same instrument as for clay analysis at a 0.01 °2θ step scanning, step time 10 s/step in the range of 3 ÷ 70 °2θ.

3.2. Grain Size

Grain size analyses have been performed on the fine fraction (<2 mm) on a Horiba Partica LA-950V2 Laser Scattering Particle Size Distribution Analyzer, in aqueous solution, after a treatment with a dispersing agent −2% extra-pure sodium polyphosphate (Na (PO3) *n*, *n* ≈ 25- Graham's salt) (Merck Millipore).

The statistical processing of the results has been carried out using the GRADISTAT package, v.8 [40]. Grain size statistical parameters have been obtained by the graphic, logarithmic method [41].

3.3. Magnetic Susceptibility

Magnetic susceptibility (k) was measured using a MFK1-FA Kappabridge (AGICO, Brno, Czech Republic) using a magnetic field of 200 A/m and 3 frequencies: F1 = 976 Hz (kF1), F2 = 3904 Hz (kF2), and F3 = 15616 Hz (kF3). Frequency dependence of magnetic susceptibility was computed using the following formulas [42]: kfd12 (%) = 100 × (kF1 − kF2)/χF1 and kfd13 (%) = 100 × (kF1 − kF3)/kF1. All magnetic susceptibility values were normalized to mass.

3.4. Chemical Composition

The concentration of a total of 60 metals was determined for 15 samples along the profile, at the Hydro-geochemistry Laboratory of the Emil Racoviță Institute of Speleology (Bucharest, Romania). The samples were dried at 60 °C, homogenized, and passed through a 2 mm sieve. The powdered samples and standard reference material (NIST 8704—Buffalo River Sediment) were digested using a microwave sample preparation system. After digestion, the solution was heated to 210 °C to evaporate the excess acid and diluted to 50 mL for subsequent analysis. The concentrations of metals were determined by inductively coupled plasma quadrupole mass spectrometry (ICP-Q-MS) using a PerkinElmer NexION 300S (PerkinElmer, Waltham, MA, USA) instrument.

In order to quantify the enrichment or depletion of certain elements throughout the soil profile, we calculated the enrichment factor (EF) [43] as follows:

$$\text{EFelement} = \frac{\frac{\text{X sample}}{\text{Ti sample}}}{\frac{\text{X background}}{\text{Ti background}}}$$

where X_{sample} is the concentration of the element (e.g., Na, K, Mg) in the sample and $X_{background}$ is the concentration of the element in the background. For the element subsoil background values, we used the FOREGS data [44] for European soils, which we consider more representative for soils than the average upper crust values [45]. We used the conservative lithogenic element Ti [46] for normalization.

3.5. Radiocarbon Dating

Radiocarbon dating of bulk organic matter in the sediment was performed on 10 samples at the AMS LMC14/ARTEMIS facility (Saclay, France) following the methods described in Dumoulin et al. [47].

A set of five more samples were prepared at the RoAMS facility hosted by the Horia Hulubei National Institute of Physics and Nuclear Engineering—NIPNE (Magurele, Romania) following the method described in Sava et al. [48]. Two of these five samples, taken from the lower part of the profile, yielded very low amounts of organic carbon and could not be measured using the method mentioned above. Root fragments from five depth intervals were also measured at NIPNE.

Inorganic carbon from sediment samples was leached with 0.5 M HCl for 96 h followed by ultrapure water rinsing, until the pH was neutralized to 5 and dried at 40 °C for 24 h.

The root fragments were first treated with 1 M HCl acid for 20 min, followed by NaOH alkali treatment for 20 min, and again a 1 M HCl acid step treatment for 1 h. All the steps were performed at 80 °C, while, in between, the samples were rinsed with ultrapure water to neutral pH. The chemical treatment was finalized with drying the samples at 60 °C for 4 h.

Both samples types were combusted and the resulting CO_2 was subsequently converted to graphite using the AGE III graphitization system, which worked in conjunction with Vario MicroCube elemental analyzer (Elementar, Langenselbold, Germany).

For the AMS measurements, all the samples were normalized to the modern radiocarbon level using the international standard NIST SRM 4990C Oxalic Acid II, while the blank level was estimated using old charcoal of unknown source. The measurement was performed on a 1 MV Tandetron^{TM} AMS system (High Voltage Engineering Europa, Amersfoort, Netherlands). The experimental data obtained for all the samples were corrected for isotopic fractionation introduced during the sample preparation and spectrometer measurement using $\delta^{13}C$. The radiocarbon ages were calculated according to Stuiver and Pollach, 1977 [49].

The age–depth model was calculated using the rbacon package [50] for the R environment [51,52], based on Intcal20 data for Northern Hemisphere atmospheric samples [53].

3.6. $\delta^{13}C$ in Soil Organic Matter

Prior to stable carbon isotope analysis, soil samples were homogenized in an agate mortar. The inorganic carbon from the samples were removed, using a modified method of Wurster et al. [54], and detailed elsewhere [9,55]. $\delta^{13}C$ values were measured at the Stable Isotope Laboratory of the Babeș-Bolyai University (Cluj-Napoca, Romania) using a Picarro Cavity Ring Down Spectroscopy analyzer [56] coupled with a combustion module (Costech Analytical Technologies, Valencia, CA, USA). All $\delta^{13}C$ values are expressed relative to VPDB using the formula $\delta^{13}C = [(Rsample/Rstandard) - 1] \times 1000$ (‰), where R is the measured $^{13}C/^{12}C$ ratio for sample and standard, respectively.

For the two-point calibration, we used atropine and acetanilide internal standards, and B2155 standard for quality assurance. The first two standards were calibrated against ANU Sucrose, B2155 Protein (Casein), and B2151 high organic standard (Elemental Microanalysis, Okehampton, UK). Each sample was measured three to four times and the average was reported. The reproducibility checked with the B2155 standard (in every run) was better than ±0.11‰ (1 s) and the accuracy of measurements was around ±0.08‰.

3.7. Optically Stimulated Luminescence (OSL) Dating

Terra rossa-type soils are widespread in this region and can be found only on limestone substrates. Two samples from such soils were taken from two exposures found some 8 km away from our site (Figure 3A,B), near the Balta village. These exposures are not in depositional context with our soil profile. A detailed description of a terra rossa-type soil close to the sampling location was given by [57].

The two clay samples were prepared at the Centre of Environmental Radioactivity and Nuclear Dating of the Babes-Bolyai University (Cluj-Napoca, Romania), where fine grain quartz (4–11 μm) was extracted following standard procedures [58]. Annual doses were determined by high resolution gamma spectrometry while for equivalent dose estimation a Risø TL/OSL-DA-20 reader was used and the single aliquot regeneration protocol was applied [59]. A detailed report on the analysis of the two samples can be found in Appendix B (Figures A1–A3 and Tables A2–A5).

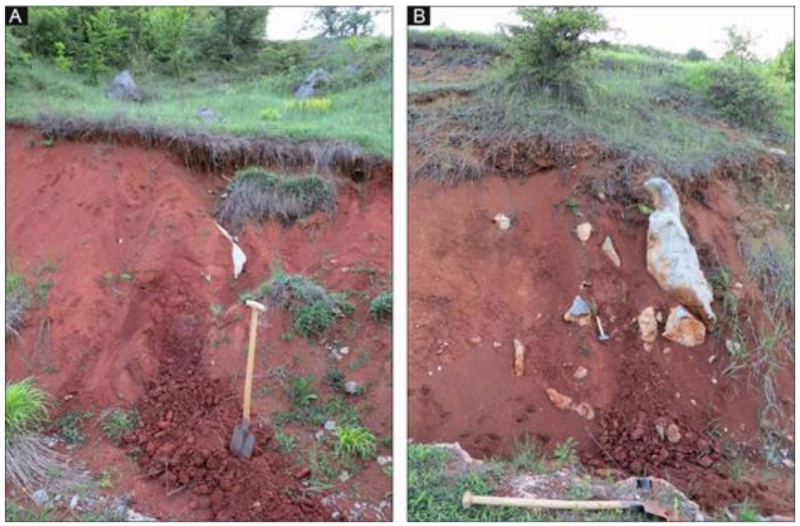

Figure 3. Terra rossa-type soil outcrops. (**A**) source of the Balta 1 OSL sample; (**B**) source of the Balta 2 OSL sample.

4. Results

4.1. POM-2 Sedimentary Sequence Description

The profile starts with a 5 cm thick organic horizon O, followed by the A horizon down to 40 cm (Figure 4). The O horizon has a dark-grey color and is characterized by high content of organic matter and a small percentage of mineral fractions. The A horizon has a lighter color and contains organic matter (roots, leaves, etc.) mixed with mineral fractions and limestone clasts. From 40 to 250 cm depth, the profile displays the characteristics of colluvium with no distinguishable horizons and a heterogeneous composition made by reddish clays mixed with detrital limestone clasts. The base of the colluvium is represented by the limestone bedrock. The horizons were characterized based on the World Reference Base for Soil Resources [60] classification.

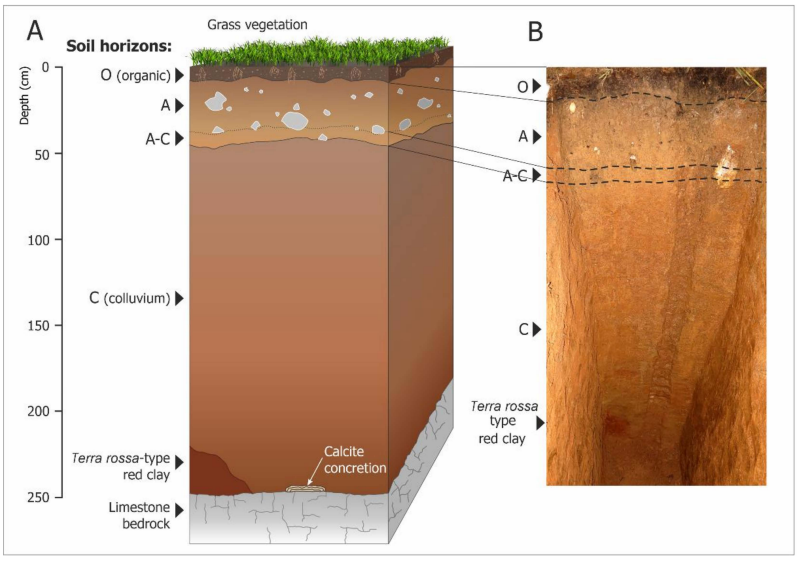

Figure 4. Schematic representation of the soil profile (**A**) and actual image of the profile (**B**). Due to the narrow dimensions of the excavation, a complete view of the profile could be seen only in perspective, hence the differences from the schematic representation which is based on measurements. A terra rossa-type soil remnant could be seen in the lower part of the profile, as well as a calcite concretion that was formed in contact with the underlying limestone.

Two interesting findings appeared at the base of the profile (Figure 4). A small 3 cm thick reddish silty carbonate concretion was found in contact with limestone possibly deposited in a former cave passage, or from carbonate-rich waters flowing at the contact between clay and limestone. Additionally, on one side of the profile, there appears a compact red clay deposit, similar to those outcropping on limestone from around this region.

4.2. Grain Size

The results of grain size analysis show that the deposit is poorly sorted, being dominated by silt with an average concentration of 64%, between a minimum percentage of 48% close to the top of the C horizon and a maximum of 80% in the A horizon (Figure 5d).

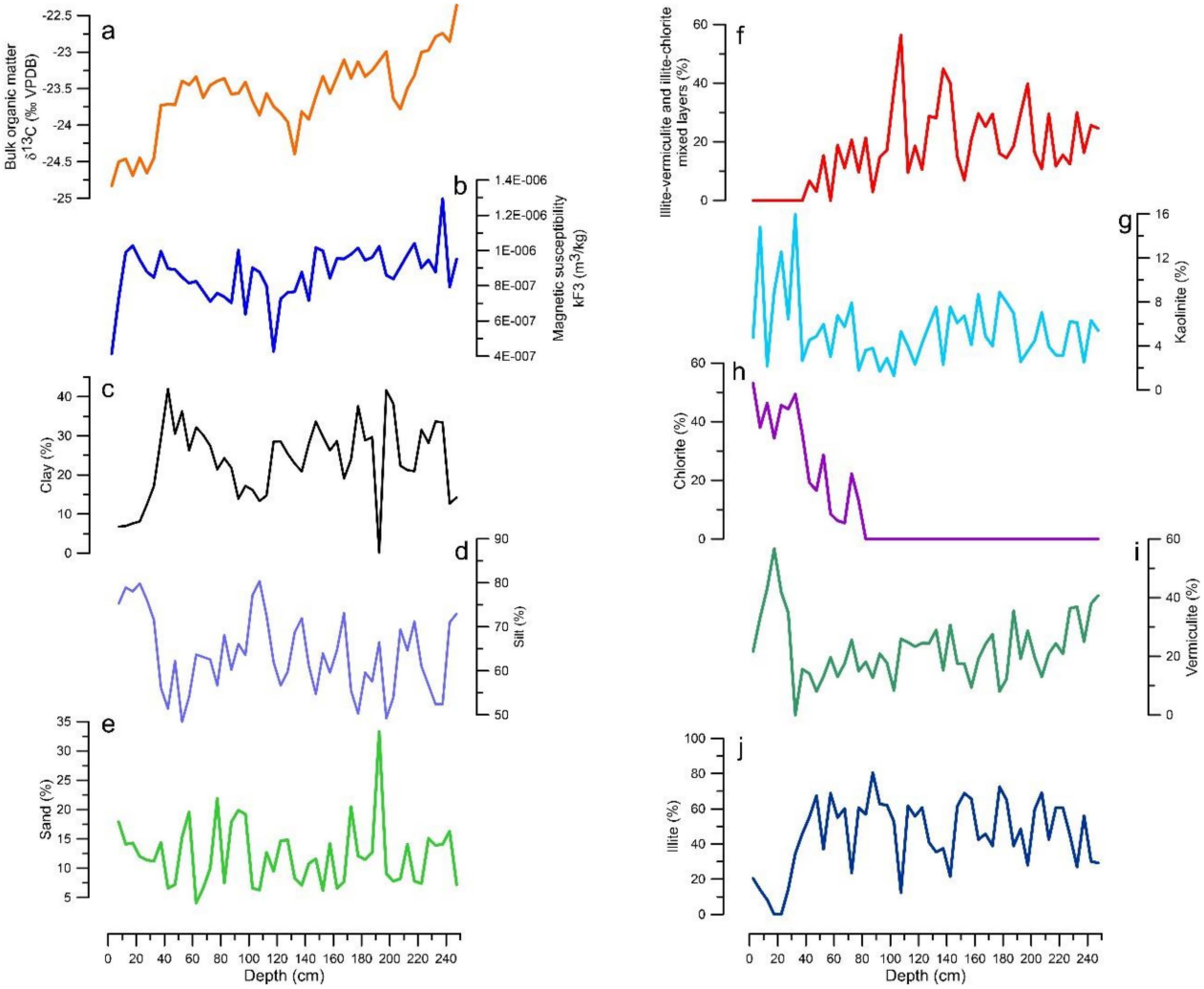

Figure 5. Variation of bulk organic matter $\delta^{13}C$ (**a**), magnetic susceptibility (**b**), grain size (**c**–**e**), and clay mineralogy (**f**–**j**) with depth.

Clay content has an average concentration of 24% and fluctuates from 0 to 42%. Along the A horizon, clay content increases from 7% to 42% at the transition towards the C horizon. Further, between depths of 40 and 100 cm, clays diminish continuously from 40% to 13%. Downwards, values display fluctuations superimposed on a shallow trend towards 30%.

Sand has the lowest values in the studied deposit with an average of 12% and displays values ranging from 4% at 62.5 cm to 33% at 187.5 cm. The maximum sand content is correlated with the loss of clay fraction, indicating a possible event characterized by higher transport energy.

4.3. Magnetic Susceptibility

Magnetic susceptibility (k) values are fluctuating across the profile between 1.3×10^{-6} and 4.14×10^{-7} m^3/kg and have an average of 8.67×10^{-7} m^3/kg. A tendency of decrease in magnetic susceptibility could be observed in the first half of the profile down to the lowest value of 4.26×10^{-7} m^3/kg at 175.5 cm depth. Downwards, the values show an increasing trend up to the highest value of 1.29×10^{-6} m^3/kg at 237.5 cm depth (Figure 5b).

The frequency dependent parameters, kfd12% and kfd13% are characterized by small values in the interval of 0 to 40 cm depth corresponding to A horizon and show minor variability except for the peaks situated at 100 cm depth where a sudden decrease could be observed. Kfd12% varies between 4.88% (at 2.5 cm depth) and 8.6% (at 237.5 cm depth) and has an average of 6.51% along the studied section, while kfd13% parameter values range between 9.85% (at 27.5 cm depth) and 13.65% (at 62.5 cm depth) with an average of 13%.

4.4. Mineralogy

The mineralogical composition of some mélange specimens collected from the cave contain quartz, calcite along with illite, and chlorite (samples AC-I, AC-II, AC-III, and AC-IV), while others (AC-V and AC-VI samples) contain quartz, plagioclase feldspar, kaolinite, chlorite, illite and vermiculite (Figure 6).

XRD patterns of the <2.0 µm fractions show a phyllosilicate association with characteristic peaks at 15 Å, 10 Å, and 7 Å areas (Figure 7), as well as quartz and feldspar. After the treatment with Mg^{2+}, POM 2-1 to POM 2-15 samples displayed a peak at 14.2 Å, while the others collapsed at ~12 Å. The treatment with EG did not produce the expansion of clay structures, peaks being situated at ~14 Å. Furthermore, saturation with K^+ maintained the $d_{(001)}$ distance at ~14 Å. This behavior excludes the presence of smectite in the analyzed samples.

Illite and vermiculite are the most quantitatively significant clay minerals found in our samples. Other phyllosilicates found are mixed layers illite–vermiculite (I/V) and illite–chlorite (I/Chl), chlorite, and kaolinite in various proportions (Table A1, Appendix A).

Illite is the most widespread mineral in the studied profile with an average of 45% (Figure 5j). Its values are fluctuating and reach a maximum of 80% (at 87.5 cm depth). In the upper part of the profile, a sudden decrease in the illite content could be observed.

Vermiculite is present along the entire length of the profile (Figure 5i) with an average percentage of ~23% and has values fluctuating from 8% (at 47.5 cm) to 56% (at 17.5 cm).

Chlorite has an average value of ~9% being present only in the upper part of the analyzed sequence until ~90 cm depth (Figure 5h), afterwards being replaced by mixed-layers structures (illite–vermiculite and illite–chlorite).

Kaolinite has the lowest content amongst the studied clays with values ranging from 1% to ~16% (at 32.5 cm) and with an average of ~6% along the profile (Figure 5g).

Mixed-layers appear starting with ~40 cm depth and have oscillating values from ~3% at 87.5 cm depth to ~40% at 197.5 cm and an average of ~17% (Figure 5f). Until ~80 cm depth, chlorite-illite structures are present, being afterwards replaced by illite–vermiculite.

In the A horizon, one can observe a change in the mineral composition, illite and mixed-layers content decreasing while chlorite, vermiculite, and kaolinite increase.

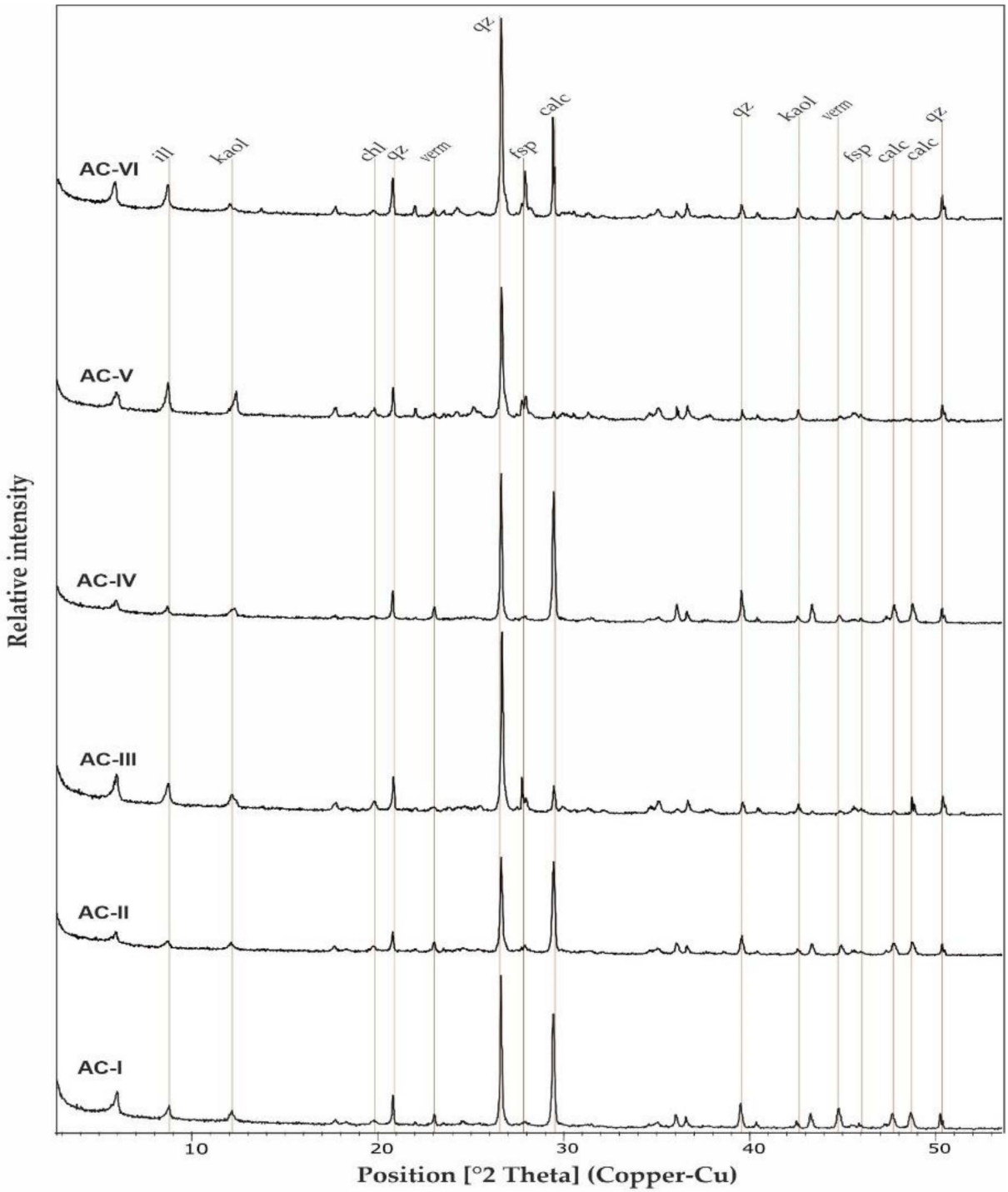

Figure 6. X-ray powder diffraction pattern of bulk rock samples: ill-illite, kaol-kaolinite, chl-chlorite, qz-quartz, verm-vermiculite, fsp-feldspar, calc-calcite.

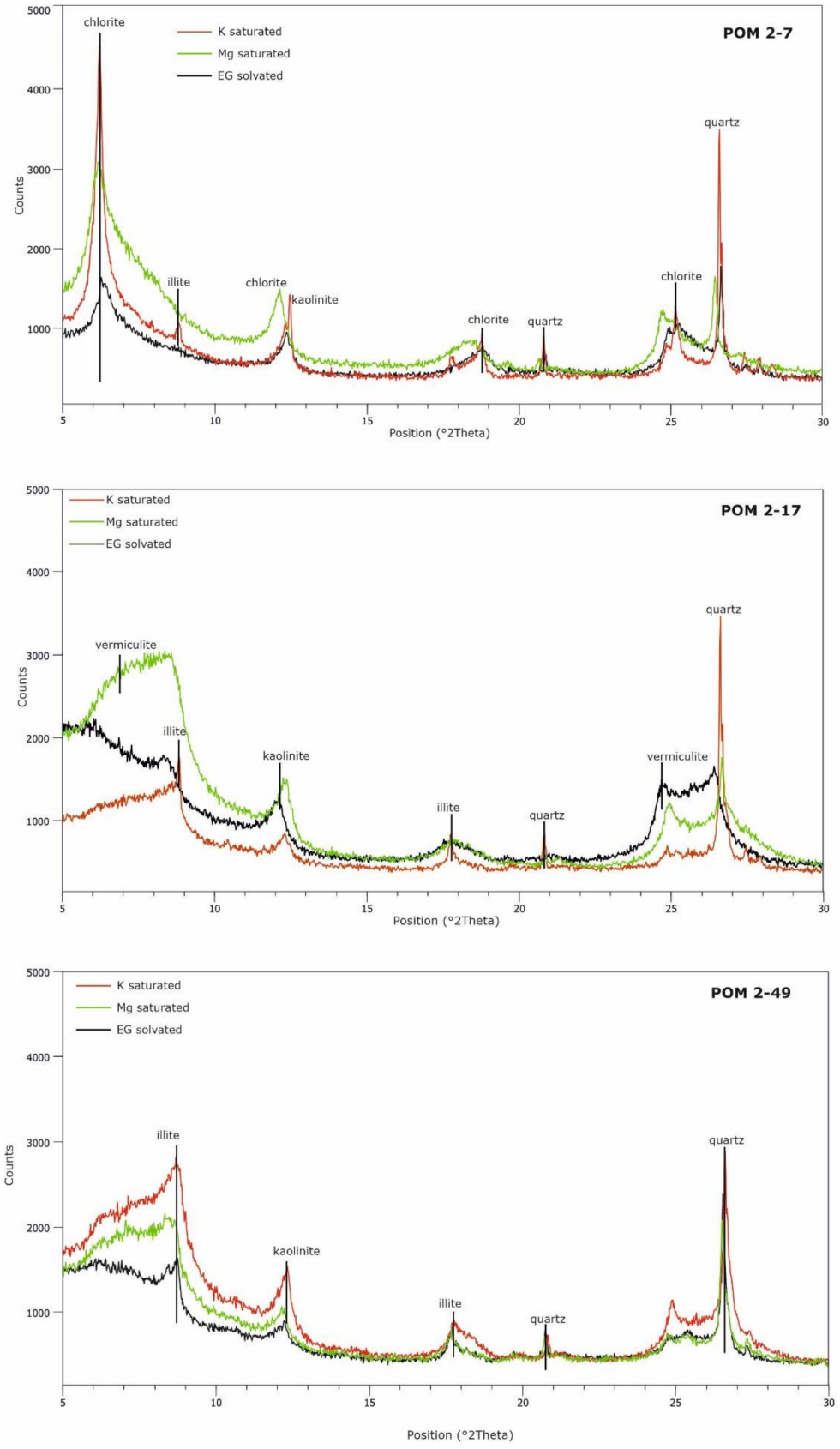

Figure 7. X-ray diffraction patterns of three selected sediment samples: POM 2-7, POM 2-17, and POM 2-49.

4.5. Chemical Composition

We present here the concentrations of a selection of 13 metals that are useful for soil description: Na, K, Mg, Ca, Sr, Ba, Cr, Mn, Fe, Zn, Al, and Si (Table 1). Ca, Mg, Sr, and Ba will also be useful in forthcoming studies for comparison with speleothems from Ascunsă Cave.

Table 1. Element concentration values of selected metals expressed in mg/kg.

Depth	Sample	Na	K	Mg	Ca	Sr	Ba	Cr	Mn	Fe	Zn	Al	Si	P
2.5	POM 2-1	2002.9	7839.8	6256.9	7495.4	42.4	358.3	80.7	328.5	35,077.5	102.5	63,525.7	100,305.3	461.7
17.5	POM 2-4	2014.1	6553.4	5600.9	7825.3	45.3	327.1	77.6	328.3	32,723.0	98.0	59,223.3	100,798.7	458.0
22.5	POM 2-5	2237.2	8242.9	6897.4	8107.8	49.0	383.6	89.9	412.6	38,570.1	119.4	70,232.6	112,078.7	453.0
27.5	POM 2-6	2122.0	8368.7	6907.2	8290.4	48.0	389.6	88.2	398.3	37,513.9	106.4	69,070.7	111,087.7	321.0
32.5	POM 2-7	1878.2	7838.4	6613.9	7965.6	39.8	382.2	79.5	516.0	36,241.2	101.9	64,258.9	93,893.8	391.3
37.5	POM 2-8	2118.2	8881.2	7475.9	9416.3	49.1	417.2	97.3	597.5	42,441.1	112.8	76,239.4	112,668.6	421.9
42.5	POM 2-9	1539.4	8818.9	7280.2	10,780.0	46.4	449.3	91.8	604.2	46,079.6	105.0	77,266.4	107,724.6	450.7
47.5	POM 2-10	1629.8	8685.0	7070.3	10,459.8	44.1	440.9	87.2	571.3	44,538.3	104.3	73,220.7	105,273.6	410.5
52.5	POM 2-11	1488.8	9816.3	7354.6	10,361.0	43.9	480.1	89.8	642.8	48,083.4	102.0	77,584.3	111,375.7	453.9
77.5	POM 2-16	1448.5	12,878.8	8292.2	11,653.1	47.5	612.2	98.1	1026.0	55,400.1	113.5	83,681.1	120,989.0	469.1
102.5	POM 2-21	1086.2	13,375.7	7843.3	11,616.6	44.3	621.3	98.7	1664.9	53,147.6	119.8	81,748.4	130,369.5	431.8
142.5	POM 2-29	1210.4	14,727.3	8589.1	11,515.0	39.6	669.3	93.5	1637.4	51,878.0	115.2	79,971.6	125,907.8	569.9
182.5	POM 2-37	1159.7	15,710.0	8430.0	12,916.1	42.8	688.5	108.8	1687.3	56,800.7	138.2	88,959.3	138,943.7	563.1
222.5	POM 2-45	1148.6	14,142.9	7859.3	12,865.7	46.4	603.7	107.7	1106.3	56,355.5	146.1	92,621.4	137,597.3	678.3
247.5	POM 2-50	1184.2	15,414.1	8338.8	10,437.5	43.6	628.5	123.2	1869.5	55,051.9	154.3	87,108.6	128,971.9	655.4

Si and Al are the most abundant, followed by Fe, K, Ca, Mg, Na, Mn, P, Ba, Zn, Cr, while Sr has the lowest concentrations. The high content of Si and Al is related to the presence of clay minerals as their basic structure is dominated by these elements.

Some elements (K, Ca, Mg, Mn, P, Ba, Zn, and Cr) tend to increase in concentration with depth while others remain constant (Si, Al, Fe, and Sr). Na displays a different behavior compared to all the other elements and shows a tendency to decrease in concentration after 50 cm depth.

The calculated EF value shows that Na, K, Mg, Ca, Sr, Cr, Si, P are depleted relative to the background level (Figure 8), while Mn, Zn, and Fe are enriched. Al, which is a major component of phyllosilicates, has an EF value of 1.

4.6. Carbon Stable Isotopes

The soil organic matter $\delta^{13}C$ values are around −24.5‰ in the O/A horizons and show an abrupt increase of almost 1‰ across the transition to the colluvium, at 40 cm depth. $\delta^{13}C$ values have a continuously decreasing trend until 130 cm, after which they start to rise slowly until 250 cm, where they reach −22.5‰. During this interval, a single large negative isotopic event can be seen between 200 and 220 cm, when values decrease by almost 1‰. Such general values are suggesting that the bulk organic matter resulted from the decomposition of a C3 plant association.

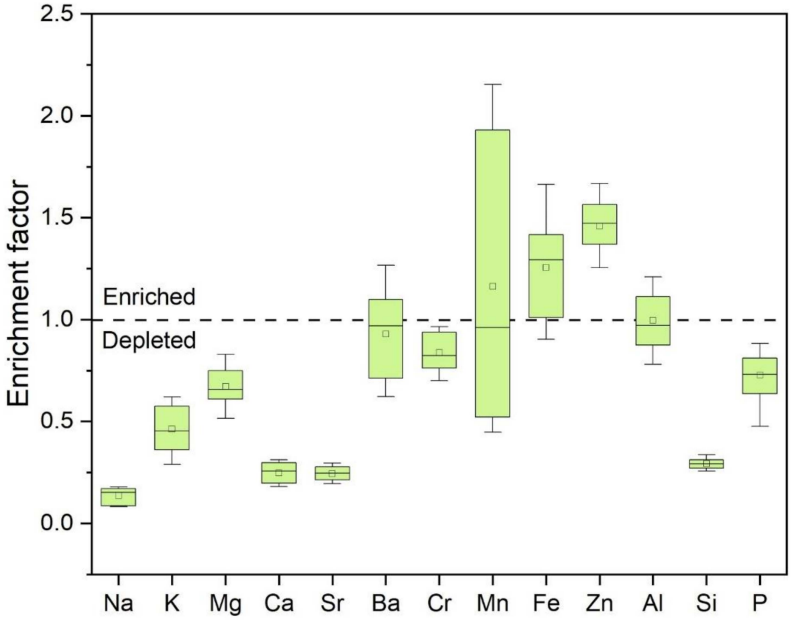

Figure 8. Enrichment factor of analyzed elements from the soil profile.

4.7. Age-Depth Model

AMS analysis returned ^{14}C ages that are in stratigraphic order, with two exceptions (Table 2). First, samples POM 2-7 and POM 2-8 is reversed, but this situation could be explained by the presence of younger organic matter in the lower sample. Secondly, and most intriguingly, the lowermost three samples analyzed (POM 2-40, POM 2-45, and POM 2-50) returned younger ages than the overlying sediment.

The age model (Figure 9) indicates an average depositional rate of 12 mm/year across the whole dataset, between a maximum of 44 mm/year and a minimum of 4 mm/year. The slowest depositional rate was recorded between ~5.4 thousands of years (kilo annum, ka) and ~2.3 ka and might indicate in fact the presence of a hiatus. Nevertheless, samples POM 2-13 and POM 2-14 (at 62.5 and 67.5 cm) are found within this slow depositional period and could be assigned to either side of the hiatus, prompting us to consider a few hundred years of uncertainty to its duration. Material from POM 2-13 has been used for dating but one cannot state whether there was an admixture of older organic matter within this sample. All five plant root samples returned modern ages.

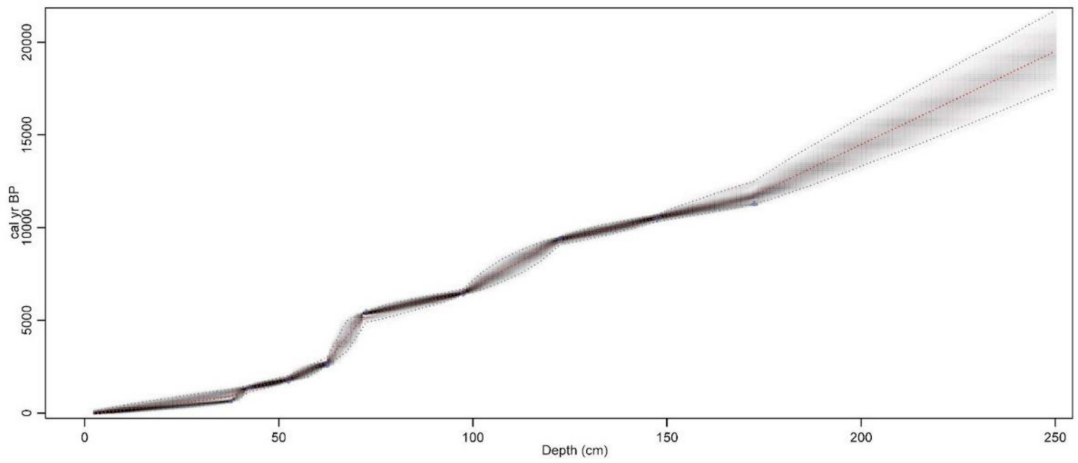

Figure 9. The age-depth model of the soil profile, with the 2σ error envelope of the calibrated ages.

Table 2. Radiocarbon ages, the calibrated years BP/AD and the dates used for construction of the age-depth model.

Sample	Laboratory	Depth (cm)	^{14}C Age Yrs BP ± Error or Remarks	^{14}C Activity ($F^{14}C$ ± Error)	Calibrated Years (BP or AD)	Date Used (BP)
			Bulk organic matter			
POM 2-7	LMC14	32.5	715 ± 30	-	717–564	641
POM 2-8	LMC14	37.5	635 ± 30	-	661–553	607
POM 2-9	ROAMS	42.5	1457 ± 52	-	1509–1284	1397
POM 2-11	ROAMS	52.5	1847 ± 45	-	1872–1621	1747
POM 2-13	ROAMS	62.5	2538 ± 35	-	2749–2494	2622
POM 2-15	LMC14	72.5	4680 ± 30	-	5476–5319	5398
POM 2-20	LMC14	97.5	5660 ± 35	-	6531–6319	6425
POM 2-25	LMC14	122.5	8380 ± 35	-	9485–9296	9391
POM 2-30	LMC14	147.5	9325 ± 40	-	10,662–10,384	10,523
POM 2-35	LMC14	172.5	9835 ± 45	-	11,391–11,186	11,289
POM 2-40	LMC14	197.5	7880 ± 35	-	8977–8559	8768
POM 2-45	LMC14	222.5	7770 ± 35	-	8629–8413	8530
POM 2-50	LMC14	247.5	6710 ± 35	-	7665–7508	7587
			Root fragments			
POM 2-9	ROAMS	42.5	modern	1.2062 ± 0.007	AD 1983–1987 (97.55%) 2σ	1985
POM 2-11	ROAMS	52.5	modern	1.1266 ± 0.008	AD 1991–1997 (97.55%) 2σ	1994
POM 2-13	ROAMS	62.5	modern	1.1752 ± 0.008	AD 1986–1990 (97.55%) 2σ	1988
POM 2-44	ROAMS	217.5	modern	1.0749 ± 0.008	AD 2001–2007 (97.55%) 2σ	2004
POM 2-49	ROAMS	242.5	modern	1.1393 ± 0.008	AD 1990–1995 (97.55%) 2σ	1993

4.8. OSL Dating

The results of the luminescence dating of the two red clay samples are presented in Table 3. The two ages are in agreement with each other within the dating uncertainty and indicate that the red clay deposits were probably formed within the Last Interglacial period.

Table 3. Results of optically stimulated luminescence dating.

SAMPLE (4–11 μm)	Equivalent Dose (Gy)	Annual Dose (Gy/ka)	Water Content (%)	Age (ka) Total Error	Random Error (%)	Systematic Error (%)
Balta 1	514 ± 10	3.85 ± 0.16	9.1 ± 0.9	127.9 ± 13.5	4.4	9.6
Balta 2	413 ± 16	2.71 ± 0.13	33 ± 3.3	143.5 ± 18.2	6.0	11.1

5. Discussion

5.1. Depositional Environment

The dominance of the fine grain fraction indicates that the sediment was transported and deposited by low energy flow [41,61] possibly from the slopes surrounding the depression. The bulk organic matter within the sediment might have also been transported from the same source area as the mineral phase.

The magnetic susceptibility signal is strongly diluted due to high concentrations of organic matter in the A horizon. The frequency dependent magnetic susceptibility signals are attributed to the ultrafine-grained superparamagnetic minerals produced by pedogenic activity [62]. A gradual increase in the magnetic susceptibility values can be observed starting around the depth of 150 cm (Figure 5). The relatively high values recorded between 40 and 250 cm suggest that an important part of the sediment originates from soil erosion. Both magnetic susceptibility and its frequency dependence suggest a change in the intensity of soil formation during the Holocene [63].

Based on the fact that many metals have negative values of the enrichment factor, it appears that the soil developed on karst terrain, with reduced silicate type sediment input.

Higher concentrations recorded for Mn and Fe are indicating a second sediment source, namely a terra rossa-type material, similar to that found incorporated in the lowest part of the profile. The silicate component is dominated by detrital clay minerals such as illite, kaolinite, and chlorite while the authigenic material is represented by vermiculite and mixed-layers structures (illite–vermiculite and illite–chlorite).

The allogenic characteristic of the illite is demonstrated by its presence in the adjacent rock formation as well as the absence of smectite from the clay association from which pedogenic illite could originate [64,65]. Kaolinite, which is inherited from the nearby rock formations, has low values in the studied soil and has no correlation with the other minerals.

Chlorite is also a detrital component in the studied deposit as formation requires higher pressure and temperature conditions than those in soil environment [66]. Chlorite values are inversely correlated with those of mixed-layers structures (r: -0.61, $p < 0.0001$). This negative correlation indicates that chlorite is in a transitional phase through mixed-layers structures [67,68].

The mélange type outcropping in the nearby area contains vermiculite, therefore two possible mechanisms could explain the presence of vermiculite in the studied profile. The first mechanism involves the transport and deposition of vermiculite from the mélange, and the second one implies a pedogenetic origin. In the A horizon, vermiculite content displays a strong negative correlation with illite (r: -0.84; $p < 0.0001$) suggesting that part of the vermiculite could originate from illite weathering.

5.2. Age and Environmental Significance of the POM 2 Soil Profile

The extrapolated age model indicates that the colluvium started depositing around 19 ka, but the period between ~11 ka and the present has better chronological constraints. The presence of modern plant roots even in the lowest part of the profile raises concerns about the contribution of modern organic matter to older sediments, with possibly unaccountable effects on radiocarbon dating.

The depositional cessation at ~5.4 ka is intriguing and we consider to have been the result of the complete removal of the mélange parent material from around the karst depression which hosts the sediment. At present, there is no mélange outcropping for several hundred meters around the site.

As the mélange was a source of mineral components, several questions arise: why deposition completely stopped, and why in the absence of an important sedimentary input did organic matter stop accumulating? As well, why did soil start forming only after 2.3 ka? Was it a completely natural phenomenon or the result of human activity?

Similar cessation events were identified in sedimentary archives from the region. For example, Cristea et al. [69] reported on a peat sequence from the alpine region of N Romania, where a very slow deposition was recorded between 6.6 ka and 3.5 ka that could be considered a hiatus. This is largely coeval with the Middle Holocene (6–4 ka), a transitional period between a wetter Early Holocene and present-day conditions.

The POM 2 stalagmite forming beneath this soil is not presenting any growth cessation over the 5.4–2.3 ka period [6], indicating that organic activity was still present at the surface and was continuing to be a source of CO_2 through microbial decomposition. There is a good fit between the variability of soil organic matter $\delta^{13}C$ and the $\delta^{13}C$ in the POM 2 stalagmite, especially since the start of soil formation at 2.3 ka (Figure 10). When comparing the extent of the isotopic variability, we can see that a ~1.5‰ decrease in organic matter values is accompanied by ~1‰ decrease in stalagmite values.

During the 6–5 ka overlapping period, the stalagmite and the soil organic matter show a trend towards higher $\delta^{13}C$ values that would be indicative of a transition to a drier hydroclimate. Such a transition, lasting between 6 and 4 ka, was previously recognized [6] based on the study of $\delta^{18}O$ values from stalagmite POM 2 and from other stalagmites in the Mediterranean realm.

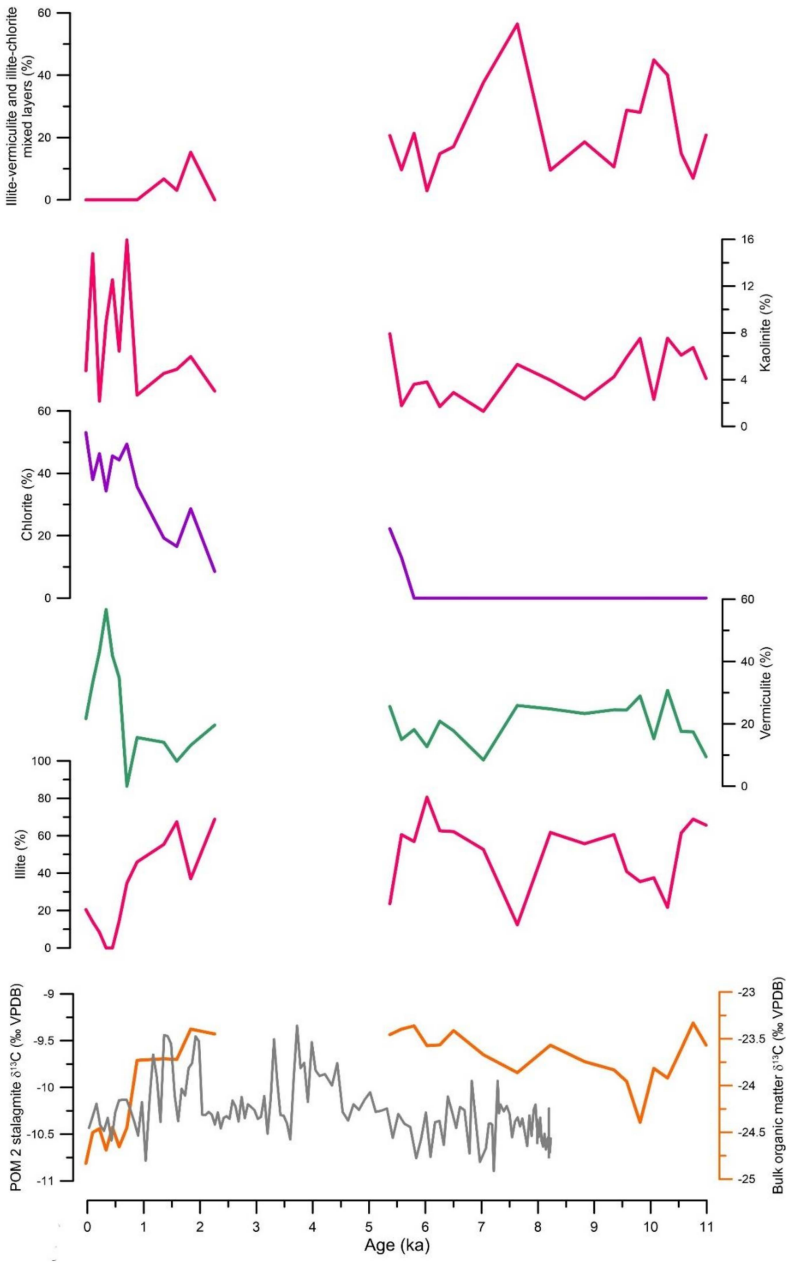

Figure 10. Variation of clays and organic matter $\delta^{13}C$ values over time: illite–vermiculite and illite–chlorite mixed layers, kaolinite, chlorite, vermiculite, illite, and $\delta^{13}C$ values.

We can thus state that the $\delta^{13}C$ values in stalagmite POM 2 are generally representative for the large-scale isotopic variability of vegetation, especially in the last two thousand years. By comparison, between 8.2 and 5.4 ka, the difference between soil organic matter and stalagmite values is larger. One possible explanation for this behavior could be that during the last 2.3 ka, isotopic disequilibrium fractionation was stronger inside Ascunsă cave than it was during the wetter Early Holocene, and led to higher isotope values of calcite. This observation could allow us, in the future, to study the variability of isotopic fractionation processes inside Ascunsă cave.

6. Conclusions

We presented here mineralogical and geochemical data from a Holocene 2.5 m deep soil profile atop Ascunsă cave (SW Romania). We performed this study in order to understand if soil environmental proxies could complement similar information obtained

from coeval stalagmites that formed in depositional connection. The studied soil originates from the erosion of a mélange complex from the vicinity of the site, whose components were transported by low energy flow, as revealed by grain size analysis. The chemical composition shows enrichment in Fe and Mn, indicating a second source of parent material, namely an underlying terra rossa-type soil.

Such soils are widespread on limestone in our study area and we attempted to obtain the first direct dates of such deposits in our region. OSL dating shows that these terra rossa-type soils were probably formed during the Last Interglacial period, some 130,000 years ago.

The clay mineralogical association of the soil profile consists of illite, chlorite, kaolinite, vermiculite and illite–vermiculite and illite–chlorite mixed-layers minerals.

Illite–chlorite-kaolinite association has a detrital origin, the source area being represented by the mélange formation and surrounding soils. Vermiculite and mixed layer minerals are the only clays formed in situ as a result of pedogenic processes.

Radiocarbon dating performed on soil organic matter shows that the sedimentary sequence has a Holocene age and recorded a depositional cessation at ~5.4 ka, most probably due to the exhaustion of the mélange parent material. Deposition recommenced at ~2.3 ka but the process behind this rejuvenation is unknown.

The basal part of the profile returned younger ages than those overlying them, due to unknown processes. However, root fragments from several depth intervals returned modern ages (including ones from the basal part of the profile). This raises important concerns about the validity of radiocarbon dating in open systems such as soil or sedimentary accumulations. Yet, it also provides an opportunity to study processes behind organic carbon incorporation in soils.

Finally, we showed that $\delta^{13}C$ values from directly connected soil–stalagmite couples could allow for the investigation of isotopic fractionation processes in caves, in order to support high resolution speleothem based paleoenvironmental studies.

Beyond its use for paleoenvironmental purposes, this study bears importance for soil development and distribution in karst areas, where it usually is discontinuous at the surface, but an important part is hosted within karst open fractures or small depressions.

Author Contributions: V.D. designed the study; V.D. and I.C.M. performed field work; L.F., D.D., B.S. and M.L.T. performed mineralogical analysis; C.M. (Constantin Marin) performed chemical analysis; C.G.P. performed rock magnetic measurements; F.L.F. performed stable carbon isotope measurements; A.T.-G. performed luminescence dating; M.I. and C.M. (Cristian Mănăilescu) performed radiocarbon dating. All authors have read and agreed to the published version of the manuscript.

Funding: Part of this work was financially supported by a grant of the Romanian Ministry of Education and Research, CNCS—UEFISCDI, project number PN-III-P4-ID-PCE-2020-2282 (ECHOES) to V.D. Part of the research leading to these results has received funding from the EEA Grants 2014–2021, under Project contract no. 3/2019. M.I. and C. Manailescu received funding from the National Programs Installations of National Interest (IOSIN) and Nucleu (PN 19 06 02 02).

Institutional Review Board Statement: Not applicable.

Informed Consent Statement: Not applicable.

Data Availability Statement: Relative content in clay minerals are given in Appendix A. Complete luminescence dating report is given in Appendix B.

Acknowledgments: The authors would like to acknowledge the AMS LMC14/ARTEMIS facility (Saclay, France) for providing radiocarbon measurements of soil organic matter. We thank J. Rethemeyer (University of Cologne, Germany) for providing initial radiocarbon dates that were the starting point of this study. We also want to thank the RoAMS technical group for the laboratory support. We would like to thank L. Maghiar for the help in preparing samples for stable isotope carbon analysis.

Conflicts of Interest: The authors declare no conflict of interest.

Appendix A

Table A1. Relative content of clay minerals of the studied profile (I/V: illite–vermiculite mixed layers; I/Chl: illite–chlorite mixed layers), values are given in %.

Sample	Depth (cm)	Illite	Vermiculite	I/Chl	Chlorite	I/V	Kaolinite
POM 2-1	2.5	20.48	21.69	-	53.07	-	4.76
POM 2-2	7.5	13.99	33.23	-	38.01	-	14.78
POM 2-3	12.5	8.35	43.17	-	46.31	-	2.16
POM 2-4	17.5	0	56.71	-	34.37	-	8.92
POM 2-5	22.5	0	41.88	-	45.58	-	12.54
POM 2-6	27.5	14.41	34.84	-	44.31	-	6.44
POM 2-7	32.5	34.66	0	-	49.39	-	15.95
POM 2-8	37.5	45.95	15.62	-	35.75	-	2.67
POM 2-9	42.5	55.36	14.1	6.7	19.24	-	4.53
POM 2-10	47.5	67.44	8.04	3.08	16.56	-	4.88
POM 2-11	52.5	36.98	13.15	15.27	28.63	-	5.97
POM 2-12	57.5	68.83	19.62	-	8.53	-	3.02
POM 2-13	62.5	55.07	13.04	18.87	6.26	-	6.76
POM 2-14	67.5	60.15	17.55	11.09	5.46	-	5.75
POM 2-15	72.5	23.65	25.57	20.64	22.23	-	7.92
POM 2-16	77.5	60.6	14.97	9.66	13	-	1.77
POM 2-17	82.5	56.88	18.16	-	-	21.36	3.6
POM 2-18	87.5	80.56	12.69	-	-	2.94	3.8
POM 2-19	92.5	62.64	20.86	-	-	14.81	1.69
POM 2-20	97.5	62.21	17.8	-	-	17.09	2.89
POM 2-21	102.5	52.67	8.41	-	-	37.62	1.29
POM 2-22	107.5	12.39	25.91	-	-	56.4	5.3
POM 2-23	112.5	61.72	24.8	-	-	9.53	3.95
POM 2-24	117.5	55.73	23.32	-	-	18.6	2.33
POM 2-25	122.5	60.62	24.52	-	-	10.61	4.24
POM 2-26	127.5	40.84	24.47	-	-	28.78	5.91
POM 2-27	132.5	35.44	28.94	-	-	28.1	7.52
POM 2-28	137.5	37.51	15.29	-	-	44.89	2.31
POM 2-29	142.5	21.67	30.73	-	-	40.05	7.54
POM 2-30	147.5	61.44	17.57	-	-	14.91	6.09
POM 2-31	152.5	68.85	17.46	-	-	6.95	6.74
POM 2-32	157.5	65.64	9.45	-	-	20.81	4.1
POM 2-33	162.5	42.53	19.2	-	-	29.59	8.68
POM 2-34	167.5	45.75	24.14	-	-	25.21	4.89
POM 2-35	172.5	38.97	27.53	-	-	29.5	4
POM 2-36	177.5	72.49	8.07	-	-	16.03	8.87
POM 2-37	182.5	65.16	12.34	-	-	14.52	7.97
POM 2-38	187.5	38.96	35.49	-	-	18.58	6.97
POM 2-39	192.5	48.5	19.21	-	-	29.72	2.57
POM 2-40	197.5	27.98	28.68	-	-	39.82	3.52
POM 2-41	202.5	59.77	19.62	-	-	16.13	4.48
POM 2-42	207.5	69.18	13.01	-	-	10.78	7.03
POM 2-43	212.5	42.56	20.95	-	-	29.54	3.95
POM 2-44	217.5	60.7	24.4	-	-	11.72	3.17
POM 2-45	222.5	60.48	20.9	-	-	15.5	3.13
POM 2-46	227.5	45.06	36.32	-	-	12.42	6.2
POM 2-47	232.5	27	36.93	-	-	29.92	6.14
POM 2-48	237.5	56.05	25.07	-	-	16.37	2.51
POM 2-49	242.5	30.1	37.97	-	-	25.61	6.32
POM 2-50	247.5	29.27	40.71	-	-	24.61	5.41

Appendix B

Luminescence dating investigations on fine (4–11 mm) quartz grains extracted from Balta 1 and Balta 2 sediment samples.

Sample preparation for luminescence measurements was performed under low-intensity red light conditions. Three days HCl (concentration of 37%) treatment was employed for carbonate removal followed by a four-day H_2O_2 (30%) treatment for organic matter removal. Wet sieving was performed in order to separate the fraction <63 µm. For fine grain fraction of quartz (4–11 µm) to be extracted, the fraction <11 µm was isolated from the grains <63 µm by settling in Atterberg cylinders according to Stokes' law. This fraction was then etched with hexafluorosilicic acid (H_2SiF_6) for 10 days. Subsequently, the removal of the grains <4 µm was carried out by centrifugation. For measurement, aliquots were prepared by pipetting a 1 mL suspension of the fine grains (2 mg of grains/1 mL acetone) onto each aluminum disc.

Annual dose determination. Radionuclide ($^{238}U/^{226}Ra$, ^{232}Th, ^{40}K) specific activities were measured using high resolution gamma-ray spectrometry and the dose rates were calculated using the conversion factors tabulated by Adamiec and Aitken [70].

Equivalent dose measurements. Luminescence measurements were performed on the standard Risø TL/OSL-DA-20 reader equipped with blue LEDs (470 ± 30 nm). IR (875 ± 80 nm) LEDs were used for infrared stimulation. Blue-light stimulated OSL signal was detected through a 7.5 mm thick Hoya U-340 UV filter. Irradiations were carried out using the incorporated 90Sr-90Y radioactive source that was calibrated against gamma-dosed calibration quartz supplied by Risø National Laboratory. A dose rate of 0.117 Gy/s for the fine quartz grain mounted on aluminium disks was obtained.

Measurement protocol: Single aliquot regeneration (SAR) applied on quartz [59,71,72]. The number of replicate measurements of the equivalent dose performed in each case varies between 12 and 16. Stimulation of the luminescence signals was evaluated from the first 0.308 s of the decay curve with an early background subtraction integrated between 1.69 s and 2.31 s. A preheat temperature of 220 °C for 10 s and a cutheat to 180 °C were employed throughout the SAR protocol. The OSL response to a fixed test dose of 17 Gy was used in the whole set of measurements to correct for sensitivity changes. At the end of each SAR cycle, a high-temperature bleach was performed by blue LED stimulation for 40 s at 280 °C.

Measurement parameters (unless otherwise mentioned): Preheat 10 s at 220 °C; Cutheat (ramp heating 5 °C/s) to 180 °C; ETOSL consisting of blue LED stimulation (36 mW/cm^2) at 280 °C for 40 s; test dose magnitude of 17 Gy; 5 regeneration doses applied to construct the dose response curve; sum of two exponentials or exponential plus linear models used for interpolating the growth curve.

Intrinsic rigor tests applied: recycling, recuperation [59,72] and IR depletion tests [73] tests have been employed to check for the suitability of these particular samples for De determination using the SAR protocol.

Table A2. Equivalent dose measurement results. The net CW-OSL signal was determined from the initial 0.308 s of the decay curve less an early background integrated between 1.69 and 2.31 s.

SAMPLE	Grain Size	No. of Aliq (Accepted/Total)	Equivalent Dose (Gy)	Recycling Ratio	IR Depleation Ratio	Recuperation (%)
Balta 1	4–11 µm	12/12	514 ± 10	1.00 ± 0.01	1.00 ± 0.01	0.03 ± 0.005
Balta 2	4–11 µm	12/16	413 ± 16	0.99 ± 0.02	0.98 ± 0.01	0.02 ± 0.05

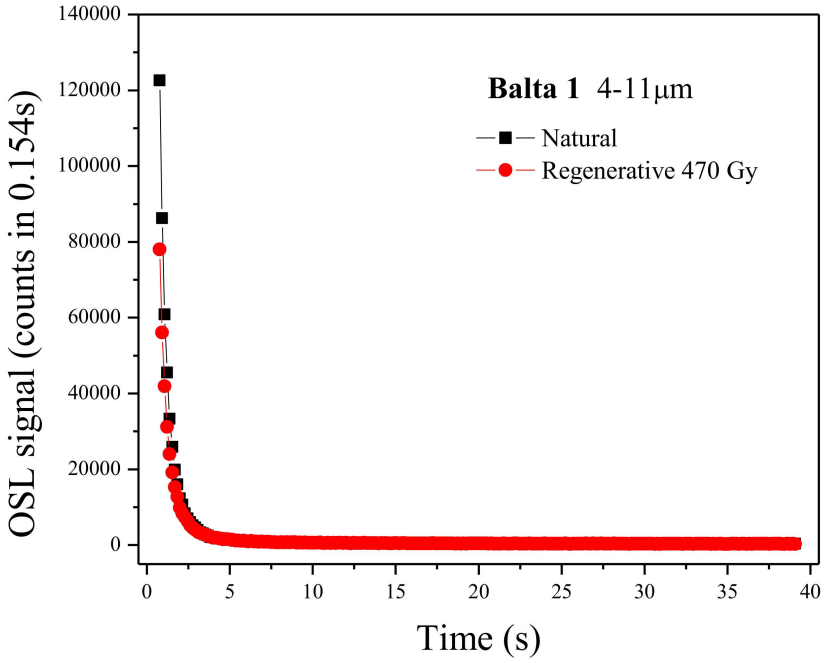

Figure A1. Typical decay curve for 4–11 μm quartz extracted from sample Balta 1.

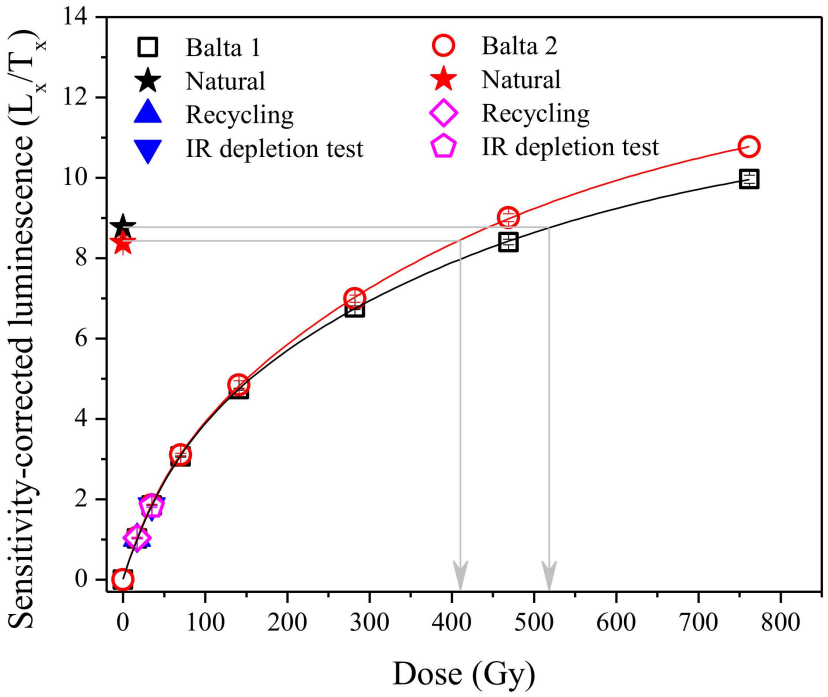

Figure A2. Average growth curves for accepted aliquots of samples Balta 1 and Balta 2.

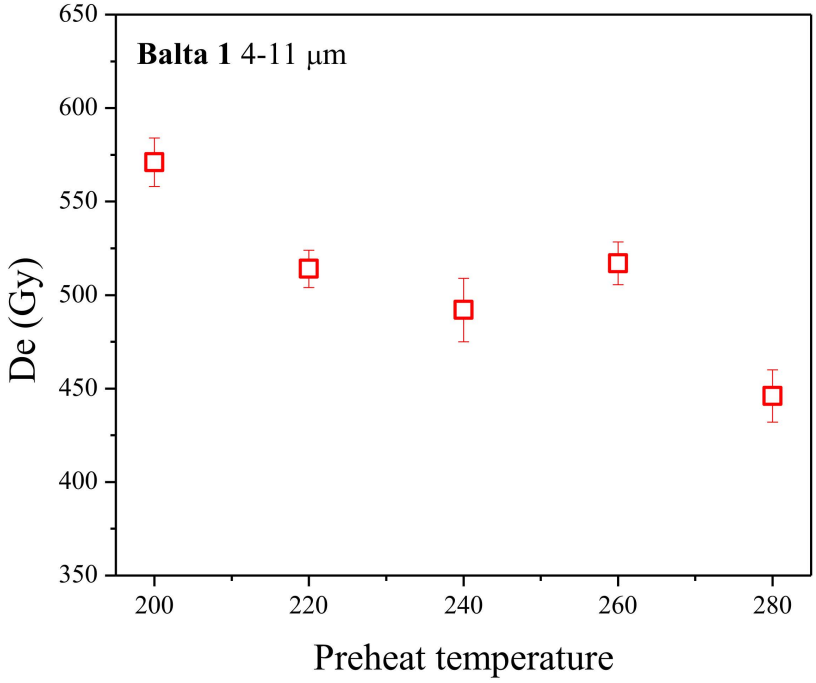

Figure A3. Preheat plateau for Balta 1 fine grains.

Table A3. Dose recovery tests results-fine grains. Given dose 533 Gy for Balta 1. Given dose 402 Gy for Balta 2.

Sample	Recovered Dose/Given Dose n = 3
Balta 1	0.93 ± 0.01
Balta 2	1.05 ± 0.11

Table A4. Radionuclide specific activity results.

Sample	Ra-226 (Bq/kg)	Th-232 (Bq/kg)	K-40 (Bq/kg)
Balta 1	36.5 ± 1.0	65.1 ± 1.9	471 ± 9
Balta 2	16.3 ± 0.9	60.3 ± 2.2	536 ± 7.9

Table A5. Age Results. Alpha efficiency factor considered was 0.04 ± 0.02.

Sample (4–11 μm)	Equivalent Dose (Gy)	Anual Dose (Gy/Ka)	Water Content (%)	Age (Ka) Total Error	Random Error (%)	Systematic Error (%)
Balta 1	514 ± 10	3.85 ± 0.16	9.1 ± 0.9	127.9 ± 13.5	4.4	9.6
Balta 2	413 ± 16	2.71 ± 0.13	33 ± 3.3	143.5 ± 18.2	6.0	11.1

The uncertainties mentioned with luminescence and data are random errors; the uncertainties mentioned with the optical ages are the overall uncertainties. All uncertainties represent 1σ (63% confidence level).

References

1. Feurdean, A.; Spessa, A.; Magyari, E.K.; Willis, K.J.; Veres, D.; Hickler, T. Trends in biomass burning in the Carpathian region over the last 15,000 years. *Quat. Sci. Rev.* **2012**, *45*, 111–125. [CrossRef]
2. Magyari, E.; Demény, A.; Buczkó, K.; Kern, Z.; Vennemann, T.; Fórizs, I.; Vincze, I.; Braun, M.; Kovacs, I.; Udvardi, B.; et al. A 13,600-year diatom oxygen isotope record from the South Carpathians (Romania): Reflection of winter conditions and possible links with North Atlantic circulation changes. *Quat. Int.* **2013**, *293*, 136–149. [CrossRef]

3. Haliuc, A.; Veres, D.; Brauer, A.; Huba, K.; Hutchinson, S.M.; Begy, R.; Braun, M. Palaeohydrological changes during the mid and late Holocene in the Carpathian area, Central-Eastern Europe. *Glob. Planet. Chang.* **2017**, *152*, 99–114. [CrossRef]
4. Onac, B.P.; Constantin, S.; Lundberg, J.; Lauritzen, S.-E. Isotopic climate record in a Holocene stalagmite from Ursilor Cave (Romania). *J. Quat. Sci.* **2002**, *17*, 319–327. [CrossRef]
5. Constantin, S.; Bojar, A.-V.; Lauritzen, S.-E.; Lundberg, J. Holocene and late Pleistocene climate in the Sub-Mediterranean continental environment: A speleothem record from Poleva Cave (Southern Carpathians, Romania). *Palaeogeogr. Palaeoclimatol. Palaeoecol.* **2007**, *243*, 322–338. [CrossRef]
6. Drăguşin, V.; Staubwasser, M.; Hoffmann, D.L.; Ersek, V.; Onac, B.P.; Veres, D. Constraining Holocene hydrological changes in the Carpathian–Balkan region using speleothem $\delta^{18}O$ and pollen-based temperature reconstructions. *Clim. Past* **2014**, *10*, 1363–1380. [CrossRef]
7. Perșoiu, A.; Onac, B.P.; Wynn, J.G.; Blaauw, M.; Ionita, M.; Hansson, M. Holocene winter climate variability in Central and Eastern Europe. *Sci. Rep.* **2017**, *7*, 1196. [CrossRef] [PubMed]
8. Bădăluţă, C.-A.; Perșoiu, A.; Ionita, M.; Piotrowska, N. Stable isotopes in cave ice suggest summer temperatures in East-Central Europe are linked to Atlantic multidecadal oscillation variability. *Clim. Past* **2020**, *16*, 2445–2458. [CrossRef]
9. Onac, B.P.; Forray, F.L.; Wynn, J.G.; Giurgiu, A.M. Guano-derived Δ13C-based paleo-hydroclimate record from Gaura Cu Musca Cave, SW Romania. *Environ. Earth Sci.* **2014**, *71*, 4061–4069. [CrossRef]
10. Cleary, D.M.; Wynn, J.G.; Ionita, M.; Forray, F.L.; Onac, B.P. Evidence of long-term NAO influence on East-Central Europe winter precipitation from a guano-derived Δ15N record. *Sci. Rep.* **2017**, *7*, 14095. [CrossRef]
11. White, W. Cave sediments and paleoclimate. *J. Cave Karst Stud.* **2007**, *69*, 76–93.
12. Lauritzen, S. Reconstructing Holocene climate records from speleothems. In *Global Change in the Holocene*, 1st ed.; Birks, J., Battarbee, R., Mackay, A., Oldfield, F., Eds.; Hodder Arnold: London, UK, 2003; pp. 242–263.
13. Wesley, L.D. *Fundamentals of Soil Mechanics for Sedimentary and Residual Soils*; John Wiley & Sons: Hoboken, NJ, USA, 2009; Chapter 1; pp. 1–11.
14. Fairchild, I.J.; Smith, C.L.; Baker, A.; Fuller, L.; Spötl, C.; Mattey, D.; McDermott, F. Modification and preservation of environmental signals in speleothems. *Earth-Sci. Rev.* **2006**, *75*, 105–153. [CrossRef]
15. Hendy, C.H. The isotopic geochemistry of speleothems—I. The calculation of the effects of different modes of formation on the isotopic composition of speleothems and their applicability as palaeoclimatic indicators. *Geochim. Cosmochim. Acta* **1971**, *35*, 801–824. [CrossRef]
16. Fohlmeister, J.; Voarintsoa, N.R.G.; Lechleitner, F.A.; Boyd, M.; Brandtstätter, S.; Jacobson, M.J.; Oster, J. Main controls on the stable carbon isotope composition of speleothems. *Geochim. Cosmochim. Acta* **2020**, *279*, 67–87. [CrossRef]
17. Gilg, H.A.; Weber, B.; Kasbohm, J.; Frei, R. Isotope geochemistry and origin of Illite-Smectite and Kaolinite from the Seilitz and Kemmlitz Kaolin deposits, Saxony, Germany. *Clay Miner.* **2003**, *38*, 95–112. [CrossRef]
18. Sheldon, N.D.; Tabor, N.J. Quantitative paleoenvironmental and paleoclimatic reconstruction using paleosols. *Earth-Sci. Rev.* **2009**, *95*, 1–52. [CrossRef]
19. Tabor, N.J.; Montañez, I.P. Oxygen and hydrogen isotope compositions of Permian Pedogenic Phyllosilicates: Development of modern surface domain arrays and implications for paleotemperature reconstructions. *Palaeogeogr. Palaeoclimatol. Palaeoecol.* **2005**, *223*, 127–146. [CrossRef]
20. Hyland, E.G.; Sheldon, N.D.; der Voo, R.V.; Badgley, C.; Abrajevitch, A. A new paleoprecipitation proxy based on soil magnetic properties: Implications for expanding paleoclimate reconstructions. *GSA Bull.* **2015**, *127*, 975–981. [CrossRef]
21. Retallack, G.J. Refining a pedogenic-carbonate CO2 paleobarometer to quantify a middle Miocene greenhouse spike. *Palaeogeogr. Palaeoclimatol. Palaeoecol.* **2009**, *281*, 57–65. [CrossRef]
22. Retallack, G.J. Pedogenic carbonate proxies for amount and seasonality of precipitation in paleosols. *Geology* **2005**, *33*, 333–336. [CrossRef]
23. Sparks, D.L. Environmental soil chemistry: An overview. In *Environmental Soil Chemistry*, 2nd ed.; Sparks, D.L., Ed.; Academic Press: Burlington, VT, USA, 2003; pp. 1–42. ISBN 978-0-12-656446-4.
24. Varela, A.N.; Raigemborn, M.S.; Richiano, S.; White, T.; Poiré, D.G.; Lizzoli, S. Late cretaceous paleosols as paleoclimate proxies of high-latitude southern hemisphere: Mata Amarilla Formation, Patagonia, Argentina. *Sediment. Geol.* **2018**, *363*, 83–95. [CrossRef]
25. Velde, B.; Meunier, A. *The Origin of Clay Minerals in Soils and Weathered Rocks*; Chapter 6; Springer: Berlin, Germany, 2008; Volume 418, pp. 283–299. [CrossRef]
26. Schulze, D.G. An Introduction to Soil Mineralogy. In *Soil Mineralogy with Environmental Applications*; John Wiley & Sons, Ltd.: Hoboken, NJ, USA, 2002; pp. 1–35. [CrossRef]
27. Bădescu, B.; Tîrlă, L. *The Karst Map of Romania*; Pro Marketing: Reșița, Romania, 2020; p. 5. (In Romanian)
28. Codarcea, A.; Răileanu, G. *Harta Geologică 1:200000, Baia de Aramă*; Institute of Geology: Bucharest, Romania, 1968.
29. Năstăseanu, S.; Bercia, I.; Iancu, V.; Hârtopanu, I. The structure of the South Carpathians (Mehedinți—Banat Area). Guide to Excursion B 2. In *Proceedings of the Carpatho-Balkan Geological Association, XII Congress*; IGR: Bucharest, Romania, 1981; pp. 1–100.
30. Mercus, D. Asupra prezenței Urgonianului în regiunea Nadanova, Podișul Mehedinților. *Comunicările Acad. R.P.R.* **1959**, *9*, 967–972.
31. Seghedi, A.; Oaie, G. Volcaniclastic turbidites of the Coşuştea Nappe: A record of late cretaceous arc volcanism in the South Carpathians (Romania). *Geol. Balc.* **2014**, *43*, 1–3.

32. Kunze, G.W.; Dixon, J.B. Pretreatment for mineralogical analysis. In *Methods of Soil Analysis*; John Wiley & Sons: Hoboken, NJ, USA, 1986; pp. 91–100. ISBN 978-0-89118-864-3.
33. Rabenhorst, M.C.; Wilding, L.P. Rapid method to obtain carbonate-free residues from limestone and petrocalcic materials. *Soil Sci. Soc. Am. J.* **1984**, *48*, 216–219. [CrossRef]
34. Dumon, M.; Van Ranst, E. PyXRD v0.6.7: A free and open-source program to quantify disordered phyllosilicates using multi-specimen X-ray diffraction profile fitting. *Geosci. Model Dev.* **2016**, *9*, 41–57. [CrossRef]
35. Biscaye, P.E. Mineralogy and sedimentation of recent deep-sea clay in the Atlantic Ocean and adjacent seas and oceans. *GSA Bull.* **1965**, *76*, 803–832. [CrossRef]
36. Brindley, G.W.; Brown, G. Crystal structures of clay minerals and their X-ray identification. *Monograph* **1980**, *5*, 495. [CrossRef]
37. Moore, D.M.; Reynolds, R.C. *X-ray Diffraction and the Identification and Analysis of Clay Minerals*, 2nd ed.; Oxford University Press: New York, NY, USA, 1997; pp. 335–339.
38. Gjems, O. Studies on clay minerals and clay-mineral formation in soil profiles in Scandinavia–norwegian Forest: Vollebekk, Norway. *Medd. Fra Det Nor. Skogforsoksves.* **1967**, *21*, 303–345.
39. Soare, B. Mineralogia Argilelor de Varsta Miopliocena din Bazinul Focsani. Ph.D. Thesis, Faculty of Geology and Geophysics, University of Bucharest, Bucharest, Romania, 2016. Unpublished.
40. Blott, S.J.; Pye, K. GRADISTAT: A grain size distribution and statistics package for the analysis of unconsolidated sediments. *Earth Surf. Process. Landf.* **2001**, *26*, 1237–1248. [CrossRef]
41. Folk, R.L.; Ward, W.C. Brazos river bar: A study in the significance of grain size parameters. *J. Sediment. Petrol.* **1957**, *27*, 3–26. [CrossRef]
42. Hrouda, F. Models of frequency-dependent susceptibility of rocks and soils revisited and broadened. *Geophys. J. Int.* **2011**, *187*, 1259–1269. [CrossRef]
43. Weiss, D.; Shotyk, W.; Appleby, P.G.; Kramers, J.D.; Cheburkin, A. Atmospheric Pb deposition since the industrial revolution recorded by five Swiss peat profiles; enrichment factors, fluxes, isotopic composition and sources K. *Environ. Sci. Technol.* **1999**, *33*, 1340–1352. [CrossRef]
44. Salminen, R.; Batista, M.J.; Bidovec, M.; Demetriades, A.; De Vivo, B.; De Vos, W.; Duris, M.; Gilucis, A.; Gregorauskiene, V.; Halamić, J.; et al. *Geochemical Atlas of Europe. Part 1: Background Information, Methodology and Maps*; Geological Survey of Finland: Espoo, Finland, 2005; p. 526.
45. Rudnick, R.L.; Gao, S. The Composition of the Continental Crust. In *Treatise on Geochemistry, The Crust*; Holland, H.D., Turekian, K.K., Eds.; Elsevier-Pergamon: Oxford, UK, 2003; Volume 3, pp. 1–64.
46. Boës, X.; Rydberg, J.; Martinez-Cortizas, A.; Bindler, R.; Renberg, I. Evaluation of conservative lithogenic elements (Ti, Zr, Al, and Rb) to study anthropogenic element enrichments in lake sediments. *J. Paleolimnol.* **2011**, *46*, 75–87. [CrossRef]
47. Dumoulin, J.-P.; Comby-Zerbino, C.; Delqué-Količ, E.; Moreau, C.; Caffy, I.; Hain, S.; Perron, M.; Thellier, B.; Setti, V.; Berthier, B.; et al. Status report on sample preparation protocols developed at the LMC14 laboratory, Saclay, France: From sample collection to 14C AMS measurement. *Radiocarbon* **2017**, *59*, 713–726. [CrossRef]
48. Sava, T.B.; Simion, C.A.; Gâza, O.; Stanciu, I.M.; Păcesilă, D.G.; Sava, G.O.; Wacker, L.; Ștefan, B.; Moșu, V.D.; Ghiță, D.G.; et al. Status report on the sample preparation laboratory for radiocarbon dating at the new Bucharest roams center. *Radiocarbon* **2019**, *61*, 649–658. [CrossRef]
49. Stuiver, M.; Polach, H. Discussion: Reporting of ^{14}C data. *Radiocarbon* **1977**, *19*, 355–363. [CrossRef]
50. Blaauw, M.; Christen, J.A. Flexible paleoclimate age-depth models using an autoregressive gamma process. *Bayesian Anal.* **2011**, *6*, 457–474. [CrossRef]
51. Kabacoff, R.I. *R in Action. Data Analysis and Graphics with R*; Manning Publications: Shelter Island, NY, USA, 2015; p. 579.
52. R Core Team. *R: A Language and Environment for Statistical Computing*; R Foundation for Statistical Computing: Vienna, Austria, 2020; Available online: https://www.R-project.org/ (accessed on 1 May 2021).
53. Reimer, P.J.; Austin, W.E.N.; Bard, E.; Bayliss, A.; Blackwell, P.G.; Bronk Ramsey, C.; Butzin, M.; Cheng, H.; Edwards, R.L.; Friedrich, M.; et al. The IntCal20 northern hemisphere radiocarbon age calibration curve (0–55 Cal KBP). *Radiocarbon* **2020**, *62*, 725–757. [CrossRef]
54. Wurster, C.M.; McFarlane, D.A.; Bird, M.I. Spatial and temporal expression of vegetation and atmospheric variability from stable carbon and nitrogen isotope analysis of bat guano in the Southern United States. *Geochim. Cosmochim. Acta* **2007**, *71*, 3302–3310. [CrossRef]
55. Forray, F.L.; Onac, B.P.; Tanţău, I.; Wynn, J.G.; Tămaş, T.; Coroiu, I.; Giurgiu, A.M. A Late holocene environmental history of a bat guano deposit from Romania: An isotopic, pollen and microcharcoal study. *Quat. Sci. Rev.* **2015**, *127*, 141–154. [CrossRef]
56. Berden, G.; Engeln, R. *Cavity Ring-Down Spectroscopy: Techniques and Applications*; John and Wiley and Sons: Hoboken, NJ, USA, 2009; p. 344.
57. Popovat, M.; Oancea, C.; Edelstein-Heller, D. Terra rossa—Un sol relict in Sud-Vestul Romaniei. *Stud. Teh. Economice. Ser. C Pedol.* **1970**, *17*, 7–19.
58. Avram, A.; Constantin, D.; Veres, D.; Kelemen, S.; Obreht, I.; Hambach, U.; Marković, S.B.; Timar-Gabor, A. Testing polymineral post-IR IRSL and quartz SAR-OSL protocols on Middle to Late Pleistocene loess at Batajnica, Serbia. *Boreas* **2020**, *49*, 615–633. [CrossRef] [PubMed]

59. Murray, A.S.; Wintle, A.G. The single aliquot regenerative dose protocol: Potential for improvements in reliability. *Radiat. Meas.* **2003**, *37*, 377–381. [CrossRef]
60. FAO and IUSS World Reference Base for Soil Resources 2014. *International Soil Classification System for Naming Soils and Creating Legends for Soil Maps—Update 2015*; World Soil Resources Reports; FAO: Rome, Italy, 2015; ISBN 978-92-5-108369-7.
61. Patterson, G.T.; Wall, G.J. Within-Pedon variability in soil properties. *Can. J. Soil Sci.* **1982**, *62*, 631–639. [CrossRef]
62. Maher, B.A.; MengYu, H.; Roberts, H.M.; Wintle, A.G. Holocene loess accumulation and soil development at the Western Edge of the Chinese Loess Plateau: Implications for magnetic proxies of palaeorainfall. *Quat. Sci. Rev.* **2003**, *22*, 445–451. [CrossRef]
63. Panaiotu, C.; Constantin, S.; Petrea, C.; Horoi, V.; Panaiotu, C.E. Rock magnetic data of late pleistocene sediments from the Pestera cu Oase and their paleoclimatic significance. In *Life and Death at the Pestera cu Oase. A Setting for Modern Human Emergence in Europe*; Trinkaus, E., Constantin, S., Zilhão, J., Eds.; Oxford University Press: Oxford, UK, 2012; p. 438. ISBN 978-0-19-539822-9.
64. Thompson, M.L.; Ukrainczyk, L. Micas. In *Soil Mineralogy with Environmental Applications*; John Wiley & Sons: Hoboken, NJ, USA, 2002; pp. 431–466. [CrossRef]
65. Wilson, M.J. The origin and formation of clay minerals in soils: Past, present and future perspectives. *Clay Miner.* **1999**, *34*, 7–25. [CrossRef]
66. Velde, B.; Meunier, A. *The Origin of Clay Minerals in Soils and Weathered Rocks*; Chapter 8; Springer: Berlin, Germany, 2008; Volume 418, pp. 322–351. [CrossRef]
67. Barnhisel, R.I.; Bertsch, P.M. Chlorites and hydroxy-interlayered vermiculite and smectite. In *Minerals in Soil Environments*; John Wiley & Sons: Hoboken, NJ, USA, 1989; pp. 729–788. ISBN 978-0-89118-860-5.
68. Egli, M.; Merkli, C.; Sartori, G.; Mirabella, A.; Plötze, M. Weathering, mineralogical evolution and soil organic matter along a Holocene soil toposequence developed on carbonate-rich materials. *Geomorphology* **2008**, *97*, 675–696. [CrossRef]
69. Cristea, G.; Cuna, S.M.; Fărcaș, S.; Tanțău, I.; Dordai, E.; Măgdaș, D.A. Carbon stable isotope composition as indicator for climatic changes during the middle and late Holocene in a peat bog from Maramureș Mountains (Romania). *Holocene* **2014**, *24*, 15–23. [CrossRef]
70. Adamiec, G.; Aitken, M. Dose rate conversion factors: Update. *Anc. TL* **1998**, *16*, 37–50.
71. Murray, A.S.; Wintle, A.G. Luminescence dating of quartz using an improved single-aliquot regenerative-dose protocol. *Radiat. Meas.* **2000**, *32*, 57–73. [CrossRef]
72. Wintle, A.G.; Murray, A.S. A review of quartz optically stimulated luminescence characteristics and their relevance in single-aliquot regeneration dating protocols. *Radiat. Meas.* **2006**, *41*, 369–391. [CrossRef]
73. Duller, G.A.T. Distinguishing quartz and feldspar in single grain luminescence measurements. *Radiat. Meas.* **2003**, *37*, 161–165. [CrossRef]